micromachines

MDPI

Article

Enhancing the Carrier Mobility and Bias Stability in Metal–Oxide Thin Film Transistors with Bilayer InSnO/a-InGaZnO Heterojunction Structure

Xiaoming Huang [1,*], Chen Chen [1], Fei Sun [1], Xinlei Chen [1], Weizong Xu [2] and Lin Li [3]

[1] College of Integrated Circuit Science and Engineering, Nanjing University of Posts and Telecommunications, Nanjing 210023, China; 1021021012@njupt.edu.cn (C.C.); 1222228325@njupt.edu.cn (F.S.); 1023223211@njupt.edu.cn (X.C.)
[2] National Laboratory of Solid State Microstructures, Nanjing University, Nanjing 210093, China; njuphyxwz@nju.edu.cn
[3] Key Laboratory of Laser Technology and Optoelectronic Functional Materials of Hainan Province, College of Physics and Electronic Engineering, Hainan Normal University, Haikou 571158, China; lin.li@hainnu.edu.cn
* Correspondence: huangxm@njupt.edu.cn

Abstract: In this study, the electrical performance and bias stability of InSnO/a-InGaZnO (ITO/a-IGZO) heterojunction thin-film transistors (TFTs) are investigated. Compared to a-IGZO TFTs, the mobility (μ_{FE}) and bias stability of ITO/a-IGZO heterojunction TFTs are enhanced. The band alignment of the ITO/a-IGZO heterojunction is analyzed by using X-ray photoelectron spectroscopy (XPS). A conduction band offset (ΔE_C) of 0.5 eV is observed in the ITO/a-IGZO heterojunction, resulting in electron accumulation in the formed potential well. Meanwhile, the ΔE_C of the ITO/a-IGZO heterojunction can be modulated by nitrogen doping ITO (ITON), which can affect the carrier confinement and transport properties at the ITO/a-IGZO heterojunction interface. Moreover, the carrier concentration distribution at the ITO/a-IGZO heterointerface is extracted by means of TCAD silvaco 2018 simulation, which is beneficial for enhancing the electrical performance of ITO/a-IGZO heterojunction TFTs.

Keywords: ITO/a-IGZO heterojunction TFTs; conduction band offset; electrical performance; TCAD silvaco simulation

Citation: Huang, X.; Chen, C.; Sun, F.; Chen, X.; Xu, W.; Li, L. Enhancing the Carrier Mobility and Bias Stability in Metal–Oxide Thin Film Transistors with Bilayer InSnO/a-InGaZnO Heterojunction Structure. *Micromachines* **2024**, *15*, 512. https://doi.org/10.3390/mi15040512

Academic Editor: Sadia Ameen

Received: 29 February 2024
Revised: 1 April 2024
Accepted: 9 April 2024
Published: 11 April 2024

1. Introduction

Over the past decade, amorphous InGaZnO (a-IGZO) thin-film transistors (TFTs) have been intensively investigated as pixel switching devices for active-matrix display applications. The competitive superiority of a-IGZO TFTs is based on the fact that they can offer high carrier mobility, high optical transparency, and low off-state leakage compared with traditional Si-based TFTs [1–3], and their manufacturing cost is lower than that of low-temperature polycrystalline silicon (LTPS) TFTs with large-area uniformity [4,5]. However, due to the high density of subgap defects existing in the bandgap of a-IGZO, the carrier mobility (μ_{FE}) and electrical stability are insufficient for advanced display applications such as AR/VR displays, flexible logic circuits, three-dimensional (3D) displays, and low-power mobile devices [6–9]. It has been reported that the subgap states mainly originate from oxygen vacancy-related defects induced by the structural disorder in a-IGZO [10], which affects the electrical properties and stability of TFTs by trapping electrons or holes in the channel layer and device interfacial region under gate bias stress, light illumination, and thermal stress [11]. To overcome this limitation of a-IGZO TFTs, the bandgap engineering of the bilayer heterojunction oxide channel has been proposed to enhance the electrical performance and bias stability of a-IGZO TFTs [12,13]. In the bilayer heterojunction structure, the improved electrical performance is caused by the large conduction band offset (ΔE_C) between two oxide channels, which will form the carrier confinement in the heterojunction

potential well due to the bandgap pinning effects [14,15]. For example, it has been reported that the InZnO/a-IGZO, InSnO/a-IGZO, and InO/a-IGZO bilayer channels all exhibit a much higher μ_{FE} than a-IGZO TFTs, which is attributed to the large difference in the Fermi energy levels of both oxide semiconductor layers. The electrons, which are the main carriers of most amorphous oxide semiconductors, are confined in the potential well constructed by the bandgap discrepancy, forming a quasi-two-dimensional electron gas (q2DEG) at the bilayer heterointerface [16–19]. In addition, it has been demonstrated that the electron trapping phenomenon could be suppressed by the formation of ΔE_C between two oxide semiconductors, enhancing the bias stress stability of heterojunction TFTs [20,21]. Since the carrier confinement and trapping in the heterojunction structure depend on the ΔE_C of both channel layers, an in-depth study of the effect of ΔE_C on carrier confinement and transport properties of heterostructure is the key to the future optimization of the electrical characteristics of heterojunction TFTs. In this study, single-active-layer a-IGZO TFTs, bilayer ITO/a-IGZO heterojunction TFTs and ITON/a-IGZO heterojunction TFTs are fabricated, and the electrical properties and positive gate bias stability of TFTs are studied. It is found that the bilayer heterojunction TFTs exhibit improvement in μ_{FE} and bias-stress stability compared with those of single-active-layer a-IGZO TFTs. The energy band alignment and band bending at the ITO/a-IGZO and ITON/a-IGZO heterojunction interface are revealed by X-ray photoelectron spectroscopy (XPS) and transmission spectra measurements. The conduction band offset (ΔE_C) is determined as 0.5 eV and 0.4 eV for the ITO/a-IGZO and ITON/a-IGZO heterojunction interface, respectively. The ΔE_C is large enough to form an architecture containing both a potential well and barrier at the heterojunction interface, which agrees with the improvement in μ_{FE} and bias-stress stability of the bilayer heterojunction TFTs. Meanwhile, it is found that the band alignment of the ITO/a-IGZO heterojunction could be modulated by N doping ITO. Lastly, the improved electrical performance of bilayer heterojunction TFTs is analyzed by TCAD simulations.

2. Device Fabrication and Simulation

In this work, the single-active-layer a-IGZO TFTs and bilayer ITO/a-IGZO heterojunction TFTs were fabricated on a heavily doped n-Si substrate with a staggered bottom-gate structure, as shown in Figure 1a,b. First, SiO_2 (200 nm) was deposited by means of plasma-enhanced chemical vapor deposition (PECVD) at T = 300 °C. The bottom ITO channel layer (3, 5, and 7 nm) was then grown using a DC-sputtering system with a plasma power of 100 W and a mixture reactive gas ratio of Ar/O_2 = 25%, and the top a-IGZO layer was continuously deposited without a vacuum break with a mixture reactive gas ratio of Ar/O_2 = 20%. The composition of the ceramic target used had an atomic ratio of In:Ga:Zn = 2:2:1. The stacked ITO/a-IGZO channel layers were fixed at 40 nm. Meanwhile, to fabricate ITON/a-IGZO heterojunction TFTs, the bottom ITON channel layer was deposited using the DC-sputtering system in a mixture of Ar, O_2 and N_2 ($Ar/O_2/N_2$ = 30 sccm/6 sccm/4 sccm) using a target of In_2O_3:Sn_2O_3 = 90:10. Next, the devices' active regions were formed by using photolithography and wet chemical etching. The Ti/Au (20/80 nm) bilayer film was deposited by means of electron-beam evaporation to form the drain/source (D/S) electrode, and a 100 nm thick SiO_2 passivation layer was deposited by means of PECVD and patterned via wet chemical etching to open the D/S contact holes. Lastly, the TFTs were formed with a channel width/length of 100 μm/20 μm and were thermally annealed in air ambient at T = 300 °C for 1 h. In addition, to measure the band offset of the ITO/a-IGZO heterointerface and the ITON/a-IGZO heterointerface, samples including a 50 nm thick a-IGZO film grown on a Corning 1737 glass substrate, a 50 nm thick ITO film grown on a Corning 1737 glass substrate, a 50 nm thick ITON film grown on a Corning 1737 glass substrate, a 4 nm thick a-IGZO film grown on a 50 nm thick ITO (ITO/a-IGZO heterojunction), and a 4 nm thick a-IGZO film grown on a 50 nm thick ITON (ITON/a-IGZO heterojunction) were characterized via X-ray photoelectron spectrometry (ULVAC-PHI from Takasaki City in Japan, PHI 5000 VersaProbe) with a monochromatic Al Kα (1486.68 eV) X-ray source.

The spectra in this study were calibrated using the absorbed C1s at a peak of 284.6 eV. The films were fabricated under the same conditions as the devices.

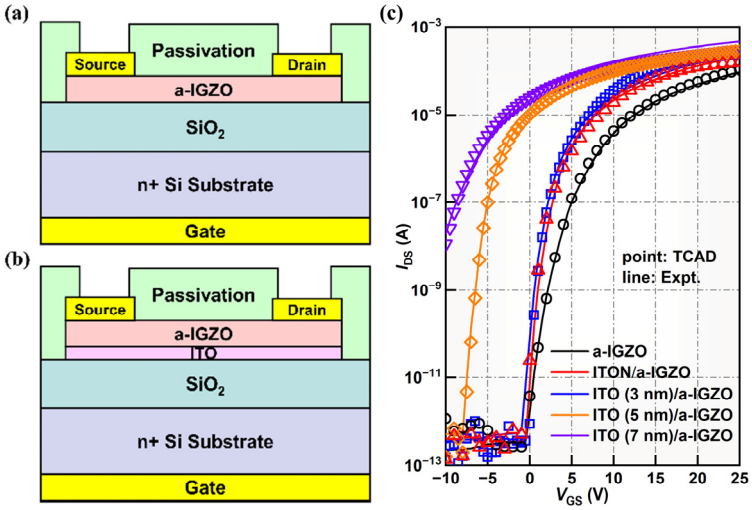

Figure 1. Schematic diagram for bottom-gate TFTs with (**a**) single-layer a-IGZO and (**b**) a ITO/a-IGZO heterojunction channel; (**c**) the transfer characteristics of the a-IGZO TFTs and ITO/a-IGZO TFTs with different ITO thicknesses. The measurement data (solid lines) fitted well with the TCAD simulation (circles).

To analyze the electrical transport mechanism of heterojunction TFTs, technology computer-aided design (TCAD) was applied to simulate a-IGZO TFTs, bilayer ITO/a-IGZO TFTs, and ITON/a-IGZO TFTs. ATLAS and Tony plot tools of the TCAD simulation were used for the carrier transport and band structure under the TFTs' operation state considering channel material properties such as electron affinity, optical bandgap, and band offset. Meanwhile, the density of states (DOS) model was used independently for both the a-IGZO and ITO layers by fitting the measured experimental data of the TFTs. The DOS in the bandgap of a-IGZO was modeled using four bands of acceptor-like tail states ($g_{TA}(E)$), acceptor-like deep-level states ($g_{GA}(E)$), donor-like tail states ($g_{TD}(E)$), and donor-like deep-level states ($g_{GD}(E)$). The DOS in the bandgap of the ITO was modeled using two bands of $g_{TA}(E)$ and $g_{TD}(E)$ [22]. The tail states were expressed by an exponential function, and the deep-level states were described by a Gaussian distribution. The specific mathematical models were as follows [23]:

$$g_{TA}(E) = N_{TA}(E) exp\left(\frac{E - E_C}{W_{TA}}\right) \quad (1)$$

$$g_{TD}(E) = N_{TD}(E) exp\left(\frac{E_V - E}{W_{TD}}\right) \quad (2)$$

$$g_{GA}(E) = N_{GA}(E) exp\left[-\left(\frac{E_{GA} - E}{W_{GA}}\right)^2\right] \quad (3)$$

$$g_{GD}(E) = N_{GD}(E) exp\left[-\left(\frac{E - E_{GD}}{W_{GD}}\right)^2\right] \quad (4)$$

where N_{TA} and N_{TD} are the effective density at the conduction band minimum (E_C) and valence band maximum (E_V), respectively. W_{TD} and W_{TA} are the characteristic slope energy of the tail states. N_{GD} and N_{GA} are the total density of the Gaussian donor and acceptor states, respectively. E_{GA} and E_{GD} are the corresponding peak energies. W_{GA} and W_{GD} are the corresponding characteristic decay energies.

3. Results and Discussions

Figure 1c shows the transfer curves of a-IGZO TFTs and ITO/a-IGZO heterojunction TFTs with different ITO thicknesses (t_{ITO}). The detailed electrical parameters of the devices, including threshold voltage (V_{th}), field effect mobility (μ_{FE}), subthreshold swing (SS), and on/off current ratio ($I_{on/off}$), are summarized in Table 1. The threshold voltage of TFTs is determined by linearly fitting the plot of the square root of drain current (I_{DS}) versus gate voltage (V_{GS}) by using the following equation:

$$I_{DS} = \frac{W\mu_{FE}C_{ox}}{2L}(V_{GS} - V_{th})^2 \quad (5)$$

where W is the channel width, L is the channel length, and C_{ox} is the capacitance per unit area of the gate dielectric. The μ_{FE} in the saturation region (V_{DS} = 10 V) is extracted by means of the normal method of the square root I_{DS} versus V_{GS} plot, and the SS is calculated via the inverse of the maximum slope of transfer curves. It is found that the ITO/a-IGZO heterojunction TFTs are transformed to the depletion mode (V_{th} = −4.9 V) when t_{ITO} increases to 5 nm, which is due to the high carrier concentration in the bottom ITO channel. As t_{ITO} increases to 7 nm, the I_{DS} of the TFTs is weakly modulated by V_{GS}. Thus, these devices are excluded in subsequent discussions. The detailed electrical parameters are listed in Table 1. It is clear that the electrical properties of bilayer ITO/a-IGZO heterojunction TFTs with a t_{ITO} of 3 nm are apparently improved compared to those of a-IGZO TFTs. For example, the μ_{FE} is increased from 6.8 $cm^2\ V^{-1}s^{-1}$ to 12.4 $cm^2\ V^{-1}s^{-1}$, and the V_{th} is reduced from 4.8 V to 2.8 V. This result may be caused by the increased carrier concentration in the total channels [17,24,25]. In contrast, the μ_{FE} of bilayer ITON/a-IGZO heterojunction TFTs is decreased when nitrogen is doped into the ITO thin film, which indicates that the carrier concentration is decreased by N doping [26,27].

Table 1. Extracted electrical parameters of the a-IGZO TFTs, ITON/a-IGZO TFTs and ITO/a-IGZO TFTs with different ITO thicknesses.

Channel Structure	V_{th} (V)	μ_{FE} ($cm^2\ V^{-1}s^{-1}$)	SS (V dec^{-1})	$I_{on/off}$
a-IGZO	4.8	6.8	0.7	$>10^8$
ITO/a-IGZO (ITO 3 nm)	2.8	12.4	0.46	$>10^8$
ITO/a-IGZO (ITO 5 nm)	−4.9	13.2	0.55	$>10^8$
ITON/a-IGZO (ITON 3 nm)	3.2	11.2	0.41	$>10^8$

The electrical stability of a-IGZO TFTs, ITO/a-IGZO TFTs and ITON/a-IGZO TFTs was tested under positive gate bias stress (PBS). The tested TFTs were stressed at V_{GS} = 20 V for 5000 s. Figure 2a–c show the evolution of transfer curves as a function of PBS duration for the a-IGZO TFTs, ITO/a-IGZO TFTs and ITON/a-IGZO TFTs, respectively. For the stressed TFTs, the transfer curves of the devices parallel shift in the positive direction, and there is a little degradation of their μ_{FE} and SS. This result agrees with previous reports indicating that moderate PBS does not considerably generate additional trap states within a-IGZO TFTs [28]. As a result, the positive threshold voltage drift (ΔV_{th}) should be attributed to the field-induced electron trapping at the channel/gate dielectric interface [29]. It is clearly observed that the ITO/a-IGZO heterojunction TFTs apparently exhibit better electrical stability compared with the a-IGZO TFTs and ITON/a-IGZO heterojunction TFTs after PBS. Correspondingly, the ΔV_{th} of the ITO/a-IGZO heterojunction TFTs (0.5 V) is lower than that of the a-IGZO TFTs (2.1 V) and ITON/a-IGZO heterojunction TFTs (0.7 V). The improved bias stability of bilayer ITO/a-IGZO heterojunction TFTs could be attributed to the suppression of the electron trapping phenomenon by the formation of an energy barrier between the ITO and a-IGZO channel layers [20,29].

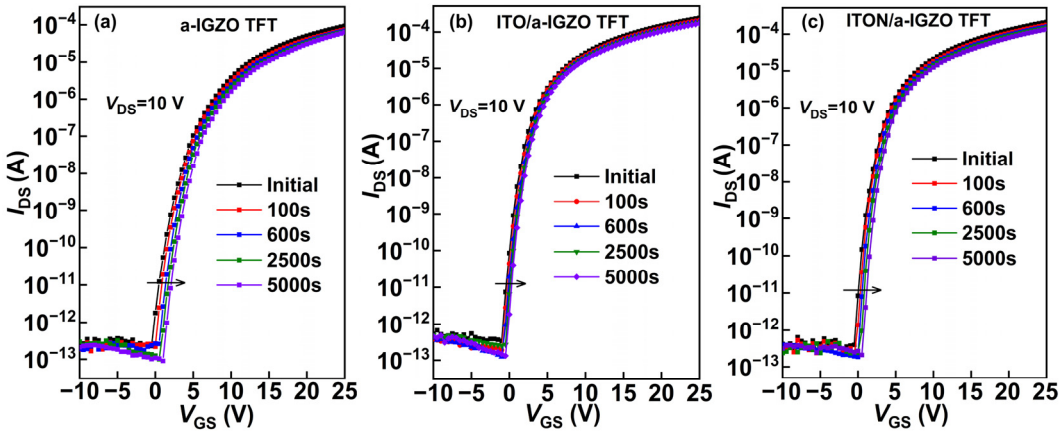

Figure 2. Evolution of the transfer curves as a function of PBS time for (**a**) a-IGZO TFTs; (**b**) ITO/a-IGZO heterojunction TFTs; (**c**) ITON/a-IGZO heterojunction TFTs.

To reveal the mechanism of the enhanced electrical performance of ITO/a-IGZO heterojunction TFTs, the energy band alignment of the ITO/a-IGZO heterointerface is analyzed using XPS and optical transmittance. In this work, the valence band offset (ΔE_V) at the heterointerface of ITO/a-IGZO is calculated by using Kraut's method based on the core-level (CL) photoelectric emission. The valence band maximum (VBM) of the samples is defined by using a linear extrapolation method. To determine the ΔE_V, the binding energy differences between the VBM and the selected core peaks for the single layers are combined with the CL binding energy differences for the heterojunction samples. Based on Kraut's model, the ΔE_V of ITO/a-IGZO heterojunction interface can be described by the following equation [30,31]:

$$\Delta E_V = \left(E_{CL}^{ITO} - E_{VBM}^{ITO}\right) - \left(E_{CL}^{IGZO} - E_{VBM}^{IGZO}\right) - \left(E_{CL}^{ITO} - E_{CL}^{IGZO}\right) \quad (6)$$

where E_{CL}^{ITO} and E_{VBM}^{ITO} are the binding energy of the selected CL peak and the valence band maximum (VBM) of the bulk ITO film, respectively; E_{CL}^{IGZO} and E_{VBM}^{IGZO} are the binding energy of the selected CL peak and the VBM of the bulk a-IGZO film, respectively; and $\left(E_{CL}^{ITO} - E_{CL}^{IGZO}\right)$ corresponds to the CL peak difference of the ITO/a-IGZO heterojunction.

Figure 3a–c show the CL spectra of Zn $2p_{3/2}$, In $3d_{5/2}$ and the VBM (inset) for the a-IGZO film, ITO film and ITON film, respectively. The VBM values of a-IGZO, ITO and ITON are calculated by linearly fitting the leading edge of the E_V and the flat energy distribution and obtaining the intersection of the two lines [32]. As shown in Figure 3a, it is found that the Zn $2p_{3/2}$ of the bulk a-IGZO film is located at 1021.55 eV, and the VBM value of 2.34 eV is deduced from the VB spectra via linear fitting as described above. Thus, the energy difference between the Zn $2p_{3/2}$ CL peak and the VBM of the bulk a-IGZO film is determined to be 1019.21 eV. The CL spectrum of In $3d_{5/2}$ and the VBM for the bulk ITO film are shown in Figure 3b. The In $3d_{5/2}$ is located at 444.3 eV, and the VBM value of 2.02 eV is deduced from the VB spectra for the bulk ITO film. As a result, the energy difference between the In $3d_{5/2}$ CL peak and the VBM is calculated to be 442.28 eV for bulk ITO film. As shown in Figure 3c, the In $3d_{5/2}$ is located at 444.42 eV, and the VBM value of 1.88 eV is deduced from the VB spectra for bulk ITON film. Therefore, the energy difference between the In $3d_{5/2}$ CL peak and the VBM is calculated to be 442.54 eV for the bulk ITON film. Furthermore, the CL spectra of Zn $2p_{3/2}$ and In $3d_{5/2}$ (inset) of the ITO/a-IGZO and ITON/a-IGZO heterojunction are shown in Figure 3d,e. Compared with the spectra of the bulk a-IGZO film, bulk ITO film and bulk ITON film, the Zn $2p_{3/2}$ CL peak and the In $3d_{5/2}$ CL peak in the ITO/a-IGZO and ITON/a-IGZO heterojunction interfaces are shifted to 1021.67 eV, 444.55 eV, and 444.67 eV, respectively. The Zn $2p_{3/2}$ CL peak position difference between the bulk a-IGZO and the ITO(N)/a-IGZO heterojunction may be due to the chemical bonding of a-IGZO with ITO(N) at the heterojunction interface. The

corresponding parameters extracted from XPS measurements are summarized in Table 2. Based on Equation (6), the values of ΔE_V for the ITO/a-IGZO and ITON/a-IGZO interfaces are determined to be 0.19 eV and 0.33 eV, respectively.

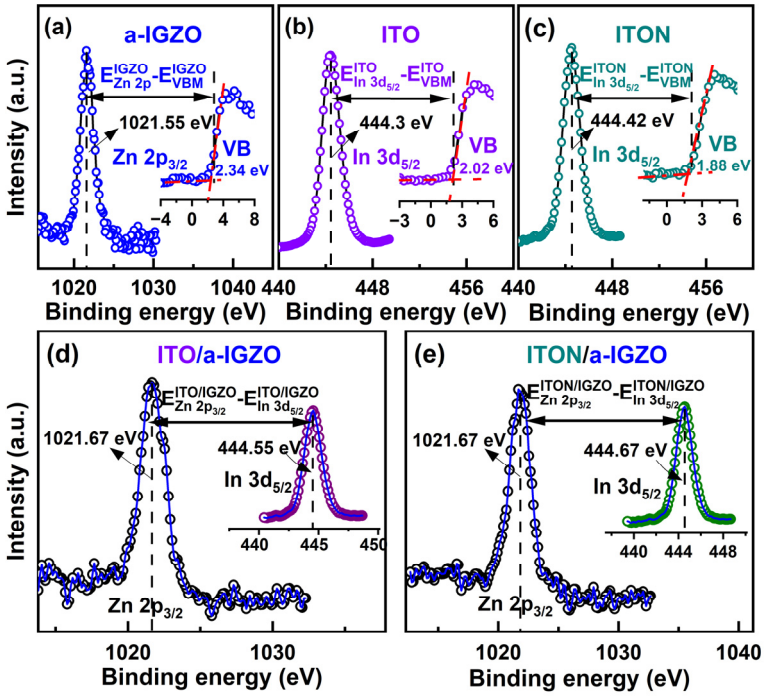

Figure 3. (**a**) Zn $2p_{3/2}$ XPS and valence band spectra of the a-IGZO film. (**b**,**c**) In $3d_{5/2}$ XPS and valence band spectra of the ITO and the ITON film, respectively. (**d**,**e**) Zn $2p_{3/2}$ and In $3d_{5/2}$ XPS spectra of the ITO/a-IGZO film and ITON/a-IGZO film, respectively.

Table 2. The binding energies (eV) of the XPS peaks and VBM for the a-IGZO, ITO, ITON, ITO/a-IGZO and ITON/a-IGZO samples.

Sample	Metal E_{CL}	Peak (Bulk)	Peak (Interface)	Peak Shift	VBM
a-IGZO	Zn $2p_{3/2}$	1021.55	1021.67	0.12	2.34
ITO	In $3d_{5/2}$	444.3	444.55	0.25	2.02
ITON	In $3d_{5/2}$	444.42	444.67	0.25	1.88

To calculate the ΔE_C values of the ITO/a-IGZO and ITON/a-IGZO heterostructures, the optical band gap (E_g) of the a-IGZO film, ITO film and ITON film grown on glass substrates are determined by sharply increasing the absorption region based on the Tauc law [33]. Figure 4a,b show the plot of $(\alpha hv)^2$ versus hv, where α, h, and v are the absorbance, Planck constant, and light frequency, respectively. The estimated E_g of the a-IGZO film, ITO film and ITON film are 3.1 eV, 3.79 eV and 3.83 eV, respectively, agreeing with previous reports [34–36]. Band-gap widening in N-doped ITO thin films can be ascribed to the reduction in the crystal lattice constant [26,37]. The ΔE_C of the ITO/a-IGZO and ITON/a-IGZO heterojunction interfaces can be estimated based on the following expression: $\Delta E_C = E_g^{ITO} - E_g^{IGZO} - \Delta E_V$. Based on this expression, the ΔE_C is deduced to be 0.5 eV and 0.4 eV for the ITO/a-IGZO and ITON/a-IGZO heterojunction interface, respectively. The comparatively large ΔE_C will form an architecture containing both a potential well and barrier at the heterojunction interface, which is helpful to accumulate carrier and suppress the electron trapping phenomenon for ITO/a-IGZO heterojunction TFTs. As a result, the calculated ΔE_C values are consistent with the results indicating that the ITO/a-IGZO TFTs exhibit a higher μ_{FE} and bias stress stability than the ITON/a-IGZO

TFTs after PBS. In addition, based on the calculated values, the energy band alignment of the ITO/a-IGZO heterojunction is shown in Figure 4c.

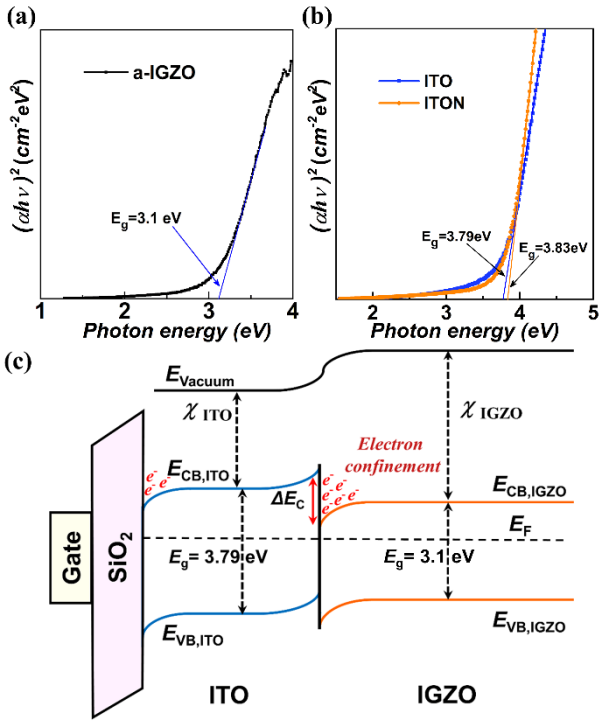

Figure 4. The calculated band gap energies for (**a**) a-IGZO films and (**b**) ITO and ITON films deposited on glass substrates. (**c**) Schematic diagram of the calculated band structure of the ITO/a-IGZO heterointerface.

To further confirm the conduction properties of the ITO/a-IGZO heterojunction TFTs, the TCAD simulation of the band structure of a-IGZO TFTs, ITO/a-IGZO heterojunction TFTs, and ITON/a-IGZO heterojunction TFTs is next carried out to quantitatively analyze the devices' transport behavior. In the simulation, the model experimental parameters are incorporated from the fabricated devices, such as the carrier mobility, optical bandgap, band offset, and permittivity. Meanwhile, the DOS model is applied independently for the a-IGZO, ITO, and ITON channel layers by fitting the measured experimental data of the TFTs. The parameters used in the TCAD simulation for a-IGZO TFTs, ITO/a-IGZO heterojunction TFTs, and ITON/a-IGZO heterojunction TFTs are summarized in Table 3. As shown in Figure 5, the carrier concentration distribution of a-IGZO TFTs, ITO/a-IGZO heterojunction TFTs, and ITON/a-IGZO heterojunction TFTs at V_{GS} = 10 V is extracted. Compared with a-IGZO TFTs, it is found that there is a high density of carriers (~2.1 × 10^{19} cm^{-3}) distributed at the ITO/a-IGZO interface for the ITO/a-IGZO heterojunction TFTs. The distribution of carriers at the ITO/a-IGZO interface is similar to that in a q2DEG system at the heterointerface [38,39], which is beneficial for decreasing carrier scattering and enhancing the μ_{FE} of heterojunction TFTs. This result agrees with the improved μ_{FE} for the ITO/a-IGZO heterojunction TFTs, which can be attributed to the increased carrier concentration in the channel. In contrast, it is found that the distributed electron concentration (~1.4 × 10^{19} cm^{-3}) at the ITON/a-IGZO interface is less than that of the ITO/a-IGZO interface, which can be attributed to the decrease in the number of electrons in the N-doped ITO channel layer [12,40,41]. Correspondingly, the μ_{FE} of the ITON/a-IGZO heterojunction TFTs is less than that of the ITO/a-IGZO heterojunction TFTs due to the decrease in carrier accumulation at the device heterojunction interface. As a result, the distributed carrier concentration at the ITO/a-IGZO interface plays an important role in modulating the electrical performance of heterojunction TFTs.

Table 3. The parameters used in the TCAD simulation for a-IGZO, ITO/a-IGZO and ITON/a-IGZO TFTs.

Parameters	a-IGZO	ITO	ITON	Description
N_{TA} ($eV^{-1}cm^{-3}$)	2.45×10^{20}	1×10^{20}	2.5×10^{20}	Accept-like tail states at E_C
W_{TA} (eV)	0.05	0.02	0.1	Conduction-band-tail slope
N_{GA} ($eV^{-1}cm^{-3}$)	3.2×10^{17}	-	-	Peak of O_i states
W_{GA} (meV)	0.44	-	-	Characteristic decay energy
E_{GA} (eV)	0.8	-	-	Peak energy
N_{TD} ($eV^{-1}cm^{-3}$)	1×10^{19}	4×10^{20}	1.5×10^{20}	Donor-like tail states at E_V
W_{TD} (eV)	0.2	0.11	0.11	Valence-band-tail slope
N_{GD} ($eV^{-1}cm^{-3}$)	6×10^{17}	-	-	Peak of Gaussian donor-like states
W_{GD} (eV)	0.3	-	-	Characteristic decay energy
E_{GD} (eV)	2.9	-	-	Peak energy
E_g (eV)	3.1	3.79	3.83	Optical band gap
ΔE_C (eV)	-	0.5 (ITO/a-IGZO)	0.4 (ITON/a-IGZO)	Conduction band offset

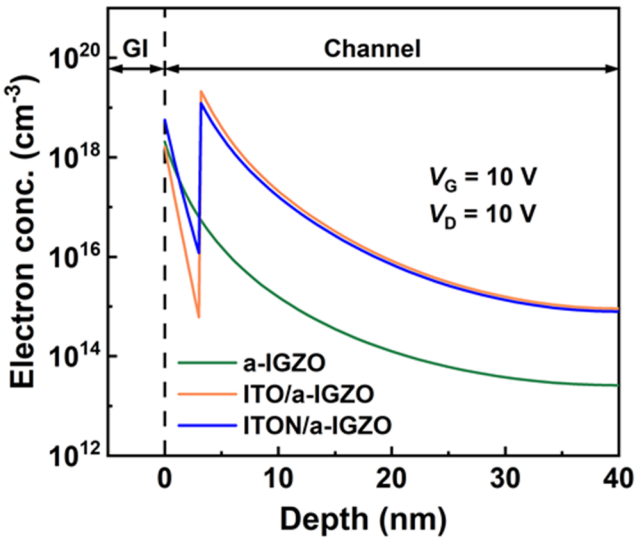

Figure 5. Simulation of the electron concentration distribution of a-IGZO TFTs, ITO/a-IGZO TFTs and ITON/a-IGZO TFTs.

4. Conclusions

In this work, bilayer ITO/a-IGZO heterojunction TFTs are designed based on the strategy of bandgap engineering. Compared to a-IGZO TFTs, the mobility (μ_{FE}) of the ITO/a-IGZO heterojunction TFTs is increased from 6.8 cm^2 $V^{-1}s^{-1}$ to 12.4 cm^2 $V^{-1}s^{-1}$, and the ΔV_{th} of the ITO/a-IGZO heterojunction TFTs is decreased from 2.1 V to 0.5 V. By means of XPS characterization, the ΔE_C of ITO/a-IGZO and ITON/a-IGZO heterojunctions has been determined to be 0.5 eV and 0.4 eV, respectively. The results indicate that the formed potential well at the ITO/a-IGZO heterointerface can cause electronic accumulation, which is beneficial for improving the μ_{FE} of the ITO/a-IGZO TFTs. Meanwhile, the comparatively large ΔE_C can effectively reduce the electron trapping phenomenon and improve the bias stress stability of heterojunction TFTs. Moreover, it is found that there is a high density of carriers distributed at the ITO/a-IGZO interface for the heterojunction TFTs via the TCAD simulation, which indicates that the distributed carrier concentration at the heterojunction interface plays a key role in determining the μ_{FE} of the heterojunction TFTs. As a result, the heterojunction channel structure will provide an approach to overcome the trade-off between μ_{FE} and bias stability in a-IGZO TFTs.

Author Contributions: Conceptualization, X.H., C.C., F.S. and X.C.; writing—original draft preparation, C.C.; writing—review and editing, X.H., C.C, F.S., W.X. and L.L. All authors have read and agreed to the published version of the manuscript.

Funding: This research was funded by the National Natural Science Foundation of China (Grant No. 62064004) and China Postdoctoral Science Foundation (Grant No. SBH19006).

Data Availability Statement: The original contributions presented in the study are included in the article, further inquiries can be directed to the corresponding author.

Conflicts of Interest: The authors declare no conflict interest.

References

1. Kamiya, T.; Nomura, K.; Hosono, H. Present status of amorphous In-Ga-Zn-O thin-film transistors. *Sci. Technol. Adv. Mater.* **2010**, *11*, 044305. [CrossRef] [PubMed]
2. Myny, K. The development of flexible integrated circuits based on thin-film transistors. *Nat. Electron.* **2018**, *1*, 30–39. [CrossRef]
3. Zhu, Y.; He, Y.; Jiang, S.; Zhu, L.; Chen, C.; Wan, Q. Indium–gallium–zinc–oxide thin-film transistors: Materials, devices, and applications. *J. Semicond.* **2021**, *42*, 031101. [CrossRef]
4. Geng, D.; Wang, K.; Li, L.; Myny, K.; Nathan, A.; Jang, J.; Kuo, Y.; Liu, M. Thin-film transistors for large-area electronics. *Nat. Electron.* **2023**, *6*, 963–972. [CrossRef]
5. Chang, T.C.; Tsao, Y.C.; Chen, P.H.; Tai, M.C.; Huang, S.P.; Su, W.C.; Chen, G.F. Flexible low-temperature polycrystalline silicon thin-film transistors. *Mater. Today Adv.* **2020**, *5*, 100040. [CrossRef]
6. Chen, Y.; Kim, H.; Lee, J.; Lee, S.; Do, Y.; Choi, M.; Jang, J. An 18.6-μm-Pitch Gate Driver Using a-IGZO TFTs for Ultrahigh-Definition AR/VR Displays. *IEEE Trans. Electron Devices* **2020**, *67*, 4929–4933. [CrossRef]
7. Zulqarnain, M.; Cantatore, E. Analog and Mixed Signal Circuit Design Techniques in Flexible Unipolar a-IGZO TFT Technology: Challenges and Recent Trends. *IEEE Open J. Circuits Syst.* **2021**, *2*, 743–756. [CrossRef]
8. Zhang, J.; Cai, W.; Wilson, J.; Ma, X.; Brownless, J.; Li, Y.; Yang, J.; Yuan, Y.; Ma, P.; Xin, Q. 8.4: Invited Paper: Oxide devices for displays and low power electronics. *SID Symp. Dig. Tech. Pap.* **2019**, *50*, 81–84. [CrossRef]
9. Meng, W.; Xu, F.; Yu, Z.; Tao, T.; Shao, L.; Liu, L.; Li, T.; Wen, K.; Wang, J.; He, L. Three-dimensional monolithic micro-LED display driven by atomically thin transistor matrix. *Nat. Nanotechnol.* **2021**, *16*, 1231–1236. [CrossRef]
10. Wolfgang, K.; Daniel, F.U.; Christian, E. Origin of subgap states in amorphous In-Ga-Zn-O. *J. Appl. Phys.* **2013**, *28*, 114. [CrossRef]
11. Vemuri, R.N.; Mathews, W.P. Investigation of defect generation and annihilation in IGZO TFTs during practical stress conditions: Illumination and electrical bias. *J. Appl. Phys.* **2013**, *46*, 4. [CrossRef]
12. Seul, H.J.; Cho, J.H.; Hur, J.S.; Cho, M.H.; Cho, M.H.; Ryu, M.T.; Jeong, J.K. Improvement in carrier mobility through band-gap engineering in atomic-layer-deposited In-Ga-Zn-O stacks. *J. Alloys Compd.* **2022**, *903*, 163876. [CrossRef]
13. Cho, M.H.; Choi, C.H.; Jeong, J.K. Comparative Study of Atomic Layer Deposited Indium-Based Oxide Transistors with a Fermi Energy Level-Engineered Heterojunction Structure Channel through a Cation Combinatorial Approach. *ACS Appl. Mater. Interfaces* **2022**, *14*, 18646–18661. [CrossRef]
14. Tai, A.-H.; Yen, C.-C.; Chen, T.-L.; Chou, C.-H.; Liu, C.W. Mobility Enhancement of Back-Channel-Etch Amorphous InGaZnO TFT by Double Layers With Quantum Well Structures. *IEEE Trans. Electron Devices* **2019**, *66*, 4188–4192. [CrossRef]
15. Faber, H.; Das, S.; Lin, Y.-H.; Pliatsikas, N.; Zhao, K.; Kehagias, T. Heterojunction oxide thin-film transistors with unprecedented electron mobility grown from solution. *Sci. Adv.* **2017**, *3*, e1602640. [CrossRef]
16. Wang, P.; Yang, H.; Li, J.; Zhang, X.; Wang, L.; Xiao, J.; Zhao, B.; Zhang, S.; Lu, L. Synergistically Enhanced Performance and Reliability of Abrupt Metal-Oxide Heterojunction Transistor. *Adv. Electron. Mater.* **2022**, *9*, 2200807. [CrossRef]
17. Hyeon, J.S.; Min, J.K.; Hyun, J.Y. Atomic Layer Deposition Process-Enabled Carrier Mobility Boosting in Field-Effect Transistors through a Nanoscale ZnO/IGO Heterojunction. *ACS Appl. Mater. Interfaces* **2020**, *12*, 33887–33898. [CrossRef]
18. He, P.; Ding, C.; Zou, X.; Li, G.; Hu, W.; Ma, C.; Flandre, D.; Iñíguez, B.; Liao, L.; Lan, L. Enhanced stability and mobility of solution-processed oxide thin-film transistors with bilayer terbium-incorporated indium oxide channel. *Appl. Phys. Lett.* **2022**, *121*, 193301. [CrossRef]
19. Park, C.-Y.; Jeon, S.-P.; Park, J.B.; Park, H.-B.; Kim, D.-H.; Yang, S.H.; Kim, G.; Jo, J.-W.; Oh, M.S.; Kim, M.; et al. High-performance ITO/a-IGZO heterostructure TFTs enabled by thickness-dependent carrier concentration and band alignment manipulation. *Ceram. Int.* **2023**, *49*, 5905–5914. [CrossRef]
20. Chiu, H.-C.; Wang, H.-C.; Luo, Y.-C.; Huang, F.-H.; Kao, H.-L.; Hsueh, K.-P. Band offsets and electrical stability characterization of Zr-doped ZnO thin-film transistors with a Gd_2O_3 gate insulator. *Microelectron. Eng.* **2014**, *118*, 20–24. [CrossRef]
21. Deng, K.; Wang, X.; Huang, S.; Jiang, Q.; Yin, H.; Fan, J.; Jing, G.; Wang, Y.; Luan, T.; Wei, K. Effective suppression of deep interface states and dielectric trapping in SiN_x/GaN metal-insulator-semiconductor structures by a SiO_xN_y interfacial layer grown by plasma-enhanced atomic layer deposition. *Appl. Surf. Sci.* **2023**, *607*, 154937. [CrossRef]
22. Stewart, K.A.; Goulíouk, V.; McGlone, J.M.; Wager, J.F. Side-by-Side Comparison of Single- and Dual-Active Layer Oxide TFTs: Experiment and TCAD Simulation. *IEEE Trans. Electron Devices* **2017**, *64*, 4131–4136. [CrossRef]

23. Hsu, C.-C.; Chen, H.-P.; Ting, W.-C. Correlation Between Carrier Concentration Distribution, I–V and C–V Characteristics of a-InGaZnO TFTs. *J. Disp. Technol.* **2016**, *12*, 328–337. [CrossRef]
24. Krausmann, J.; Sanctis, S.; Engstler, J.; Luysberg, M.; Bruns, M.; Schneider, J.J. Charge Transport in Low-Temperature Processed Thin-Film Transistors Based on Indium Oxide/Zinc Oxide Heterostructures. *ACS Appl. Mater. Interfaces* **2018**, *10*, 20661–20671. [CrossRef] [PubMed]
25. Ji, X.; Yuan, Y.; Yin, X.; Yan, S.; Xin, Q.; Song, A. High-Performance Thin-Film Transistors With Sputtered IGZO/Ga_2O_3 Heterojunction. *IEEE Trans. Electron Devices* **2022**, *69*, 6783–6788. [CrossRef]
26. Tian, L.; Cheng, G.; Wang, H.; Wu, Y.; Zheng, R.; Ding, P. Effect of nitrogen doping on the structural, optical and electrical properties of indium tin oxide films prepared by magnetron sputtering for gallium nitride light emitting diodes. *Superlattices Microstruct.* **2017**, *101*, 261–270. [CrossRef]
27. Yang, S.; Zhang, C.; Yang, Z.; Yao, J.; Wang, H.; Ding, G. Effect of nitrogen doping temperature on the resistance stability of ITO thin films. *J. Alloys Compd.* **2019**, *778*, 90–96. [CrossRef]
28. Suresh, A.; Muth, J.F. Bias stress stability of indium gallium zinc oxide channel based transparent thin film transistors. *Appl. Phys. Lett.* **2008**, *92*, 033502. [CrossRef]
29. Kim, H.; Kim, S.; Yoo, J.; Oh, C.; Kim, B.; Hwang, H.; Park, J.; Choi, P.; Song, J.; Im, K.; et al. Conduction band offset-dependent induced threshold voltage shifts in a-InGaZnO TFTs under positive bias illumination stress. *AIP Adv.* **2021**, *11*, 035312. [CrossRef]
30. Carey, P.H.; Ren, F.; Hays, D.C.; Gila, B.P.; Pearton, S.J.; Jang, S.; Kuramata, A. Valence and conduction band offsets in AZO/Ga_2O_3 heterostructures. *Vacuum* **2017**, *141*, 103–108. [CrossRef]
31. Zhang, Y.Y.; Qian, L.X.; Liu, X.Z. Determination of the Band Alignment of a-IGZO/a-IGMO Heterojunction for High-Electron Mobility Transistor Application. *Phys. Status Solidi (RRL)-Rapid Res. Lett.* **2017**, *11*, 1700251. [CrossRef]
32. He, G.; Chen, X.F.; Lv, J.G.; Fang, Z.B.; Liu, Y.M.; Zhu, K.R.; Sun, Z.Q.; Liu, M. Band offsets in HfTiO/$InGaZnO_4$ heterojunction determined by X-ray photoelectron spectroscopy. *J. Alloys Compd.* **2015**, *642*, 172–176. [CrossRef]
33. Kim, H.; Gilmore, C.M.; Piqué, A.; Horwitz, J.S.; Mattoussi, H.; Murata, H.; Kafafi, Z.H.; Chrisey, D.B. Electrical, optical, and structural properties of indium–tin–oxide thin films for organic light-emitting devices. *J. Appl. Phys.* **1999**, *86*, 6451–6461. [CrossRef]
34. Chuang, C.; Fung, T.; Mullins, B.G.; Nomura, K.; Kamiya, T.; Shieh, H.D. P-13: Photosensitivity of amorphous IGZO TFTs for active-matrix flat-panel displays. *SID Symp. Dig. Tech. Pap.* **2008**, *39*, 1215–1218. [CrossRef]
35. Wu, K.-R.; Yeh, C.-W.; Hung, C.-H.; Cheng, L.-H.; Chung, C.-Y. Photoelectrochemical properties of nitrogen-doped indium tin oxide thin films prepared by reactive DC magnetron sputtering. *Thin Solid Film.* **2009**, *518*, 1581–1584. [CrossRef]
36. Avelar-Muñoz, F.; Berumen, J.A.; Aguilar-Frutis, M.A.; Araiza, J.J.; Ortega, J.J. Enhancement on carrier mobility in amorphous indium tin oxynitride (ITON) thin films. *J. Alloys Compd.* **2020**, *835*, 155353. [CrossRef]
37. Thirumoorthi, M.; Thomas Joseph Prakash, J. Structure, optical and electrical properties of indium tin oxide ultra thin films prepared by jet nebulizer spray pyrolysis technique. *J. Asian Ceram. Soc.* **2018**, *4*, 124–132. [CrossRef]
38. Cai, W.; Li, M.; Lu, S.; Qian, Q.; Zang, Z. Heterojunction Channel Engineering in Performance Enhancement of Solution-Processed Oxide Thin-Film Transistors. *IEEE Trans. Electron Devices* **2023**, *70*, 3085–3091. [CrossRef]
39. Khim, D.; Lin, Y.H.; Anthopoulos, T.D. Impact of Layer Configuration and Doping on Electron Transport and Bias Stability in Heterojunction and Superlattice Metal Oxide Transistors. *Adv. Funct. Mater.* **2019**, *29*, 1902591. [CrossRef]
40. Park, J.W.; Kang, B.H.; Kim, H.J. A Review of Low-Temperature Solution-Processed Metal Oxide Thin-Film Transistors for Flexible Electronics. *Adv. Funct. Mater.* **2019**, *30*, 1904632. [CrossRef]
41. Sun, Q.-J.; Wu, J.; Zhang, M.; Yuan, Y.; Gao, X.; Wang, S.-D.; Tang, Z.; Kuo, C.-C.; Yan, Y. Enhanced Electrical Performance and Bias-Stress Stability of Solution-Processed Bilayer Metal Oxide Thin-Film Transistors. *Phys. Status Solidi (A)* **2022**, *219*, 2200311. [CrossRef]